Multi-spectral materials: hybridisation of optical plasmonic filters, a mid infrared metamaterial absorber and a terahertz metamaterial absorber

James Grant,* Iain J. H. McCrindle, and David R. S. Cumming

Microsystems Technology Group, School of Engineering, University of Glasgow, G12 8LT, UK
**james.grant@glasgow.ac.uk*

Abstract: Multi-spectral imaging systems typically require the cumbersome integration of disparate filtering materials and detectors in order to operate simultaneously in multiple spectral regions. Each distinct waveband must be detected at different spatial locations on a single chip or by separate chips optimised for each band. Here, we report on a single component that optically multiplexes visible, Mid Infrared (4.5 μm) and Terahertz (126 μm) radiation thereby maximising the spectral information density. We hybridise plasmonic and metamaterial structures to form a device capable of simultaneously filtering 15 visible wavelengths and absorbing Mid Infrared and Terahertz. Our synthetic multi-spectral component could be integrated with silicon complementary metal-oxide semiconductor technology where Si photodiodes are available to detect the visible radiation and micro-bolometers available to detect the Infrared/Terahertz and render an inexpensive, mass-producible camera capable of forming coaxial visible, Infrared and Terahertz images.

OCIS codes: (160.3918) Metamaterials; (040.2235) Far infrared or terahertz; (310.6628) Subwavelength structures, nanostructures; (240.6680) Surface plasmons.

References and links

1. S. Kong, J. Heo, F. Boughorbel, Y. Zheng, B. Abidi, A. Koschan, M. Yi, and M. Abidi, "Multiscale fusion of visible and thermal IR Images for illumination-invariant face recognition," Int. J. Comput. Vis. **71**(2), 215–233 (2007).
2. A. L. Chan and S. R. Schnelle, "Fusing concurrent visible and infrared videos for improved tracking performance," Opt. Eng. **52**(1), 017004 (2013).
3. S. Chaudhuri and K. Kotwal, *Hyperspectral Image Fusion* (Springer, 2013).
4. M. Kowalski, M. Kastek, H. Polakowski, N. Palka, M. Piszczek, and M. Szustakowski, "Multispectral concealed weapon detection in visible, infrared, and terahertz," Proc. SPIE **9102**, 91020T (2014).
5. M. Perenzoni, N. Massari, D. Stoppa, S. Pocas, B. Delplanque, J. Meilhan, F. Simoens, and W. Rabaud, "A 160x160-pixel image sensor for multispectral visible, infrared and terahertz detection," Proceedings of *ESSCIRC* (2012), pp. 93–96.
6. H. Kang, H. Jung, and H. Lee, "Independently alterable synthetic multispectral metamaterial filter based on etalon structure," Adv. Opt. Mater. **3**(6), 774–778 (2015).
7. J. Grant, I. J. H. McCrindle, C. Li, and D. R. S. Cumming, "Multispectral metamaterial absorber," Opt. Lett. **39**(5), 1227–1230 (2014).
8. I. J. H. McCrindle, J. P. Grant, L. C. P. Gouveia, and D. R. S. Cumming, "Infrared plasmonic filters integrated with an optical and terahertz multi-spectral material," Phys. Status Solidi **212**, 1–9 (2015).
9. I. J. H. McCrindle, J. Grant, T. D. Drysdale, and D. R. S. Cumming, "Multi-Spectral materials: hybridisation of optical plasmonic filters and a terahertz metamaterial absorber," Adv. Opt. Mater. **2**(2), 149–153 (2014).
10. I. J. H. McCrindle, J. Grant, T. D. Drysdale, and D. R. S. Cumming, "Hybridization of optical plasmonics with terahertz metamaterials to create multi-spectral filters," Opt. Express **21**(16), 19142–19152 (2013).
11. T. W. Ebbesen, H. J. Lezec, H. F. Ghaemi, T. Thio, and P. A. Wolff, "Extraordinary optical transmission through sub-wavelength hole arrays," Nature **391**(6668), 667–669 (1998).
12. C. Genet and T. W. Ebbesen, "Light in tiny holes," Nature **445**(7123), 39–46 (2007).
13. Q. Chen and D. R. S. Cumming, "High transmission and low color cross-talk plasmonic color filters using triangular-lattice hole arrays in aluminum films," Opt. Express **18**(13), 14056–14062 (2010).

#254706 Received 30 Nov 2015; revised 26 Jan 2016; accepted 5 Feb 2016; published 10 Feb 2016

14. D. Inoue, A. Miura, T. Nomura, H. Fujikawa, K. Sato, N. Ikeda, D. Tsuya, Y. Sugimoto, and Y. Koide, "Polarization independent visible color filter comprising an aluminum film with surface-plasmon enhanced transmission through a subwavelength array of holes," Appl. Phys. Lett. **98**(9), 093113 (2011).
15. K. Walls, Q. Chen, S. Collins, D. R. S. Cumming, and T. D. Drysdale, "Automated design, fabrication, and characterization of color matching plasmonic filters," IEEE Photonics Tech. Lett. **24**(7), 602–604 (2012).
16. Q. Chen, D. Das, D. Chitnis, K. Walls, T. D. Drysdale, S. Collins, and D. R. S. Cumming, "A CMOS image sensor integrated with plasmonic colour filters," Plasmonics **7**(4), 695–699 (2012).
17. S. Yokogawa, S. P. Burgos, and H. A. Atwater, "Plasmonic color filters for CMOS image sensor applications," Nano Lett. **12**(8), 4349–4354 (2012).
18. Y. Huo, C. C. Fesenmaier, and P. B. Catrysse, "Microlens performance limits in sub-2μm pixel CMOS image sensors," Opt. Express **18**(6), 5861–5872 (2010).
19. J. B. Pendry, A. J. Holden, W. J. Stewart, and I. Youngs, "Extremely low frequency plasmons in metallic mesostructures," Phys. Rev. Lett. **76**(25), 4773–4776 (1996).
20. J. B. Pendry, A. J. Holden, D. J. Robbins, and W. J. Stewart, "Magnetism from conductors and enhanced nonlinear phenomena," IEEE Trans. Microw. Theory **47**(11), 2075–2084 (1999).
21. W. J. Padilla, M. T. Aronsson, C. Highstrete, M. Lee, A. J. Taylor, and R. D. Averitt, "Electrically resonant terahertz metamaterials: Theoretical and experimental investigations," Phys. Rev. B **75**(4), 041102 (2007).
22. P. R. West, S. Ishii, G. V. Naik, N. K. Emani, V. M. Shalaev, and A. Boltasseva, "Searching for better plasmonic materials," Laser Photonics Rev. **4**(6), 795–808 (2010).
23. N. I. Landy, C. M. Bingham, T. Tyler, N. Jokerst, D. R. Smith, and W. J. Padilla, "Design, theory, and measurement of a polarization-insensitive absorber for terahertz imaging," Phys. Rev. B **79**(12), 125104 (2009).
24. H. Tao, N. I. Landy, C. M. Bingham, X. Zhang, R. D. Averitt, and W. J. Padilla, "A metamaterial absorber for the terahertz regime: design, fabrication and characterization," Opt. Express **16**(10), 7181–7188 (2008).
25. J. Grant, Y. Ma, S. Saha, L. B. Lok, A. Khalid, and D. R. S. Cumming, "Polarization insensitive terahertz metamaterial absorber," Opt. Lett. **36**(8), 1524–1526 (2011).
26. X. Liu, T. Starr, A. F. Starr, and W. J. Padilla, "Infrared Spatial and Frequency Selective Metamaterial with Near-Unity Absorbance," Phys. Rev. Lett. **104**(20), 207403 (2010).
27. D. Shrekenhamer, W. Xu, S. Venkatesh, D. Schurig, S. Sonkusale, and W. J. Padilla, "Experimental realization of a metamaterial detector focal plane array," Phys. Rev. Lett. **109**(17), 177401 (2012).
28. Y. Ma, Q. Chen, J. Grant, S. C. Saha, A. Khalid, and D. R. S. Cumming, "A terahertz polarization insensitive dual band metamaterial absorber," Opt. Lett. **36**(6), 945–947 (2011).
29. J. Grant, Y. Ma, S. Saha, A. Khalid, and D. R. S. Cumming, "Polarization insensitive, broadband terahertz metamaterial absorber," Opt. Lett. **36**(17), 3476–3478 (2011).
30. J. Grant, I. Escorcia-Carranza, C. Li, I. J. H. McCrindle, J. Gough, and D. R. S. Cumming, "A monolithic resonant terahertz sensor element comprising a metamaterial absorber and micro-bolometer," Laser Photonics Rev. **7**(6), 1043–1048 (2013).
31. I. E. Carranza, J. Grant, J. Gough, and D. R. S. Cumming, "Metamaterial-based terahertz imaging," IEEE Trans. THz Sci. Technol. **5**(6), 1–10 (2015).
32. Y. Q. Ye, Y. Jin, and S. He, "Omnidirectional, polarization-insensitive and broadband thin absorber in the terahertz regime," J. Opt. Soc. Am. B **27**(3), 498–504 (2010).
33. http://www.lumerical.com/tcad-products/fdtd/, "Lumerical FDTD", retrieved http://www.lumerical.com/tcad-products/fdtd/.
34. F. A. Jenkins and H. E. White, *Fundamentals of Optics* (McGraw-Hill, 1981).
35. E. D. Palik, *Handbook of Optical Constants of Solids,* Vols. I, II, III (Elsevier Science & Tech, 1985).
36. F. Iacona, G. Ceriola, and F. La Via, "Structural properties of SiO2 films prepared by plasma-enhanced chemical vapor deposition," Mat. Sci. Semi. Proc. **4**, 43–46 (2001).
37. I. Pupeza, R. Wilk, and M. Koch, "Highly accurate optical material parameter determination with THz time-domain spectroscopy," Opt. Express **15**(7), 4335–4350 (2007).

1. Introduction

Multi-spectral imaging using visible, Infrared (IR) and Terahertz (THz) radiation is a burgeoning topic in the field of remote sensing. Each spectrally distinct waveband can provide complementary information of a particular scene via different contrast mechanisms. Visible can replicate what the human eye can see, IR can penetrate through smoke, cloud and fog while THz can penetrate non-conductive materials such as plastic and clothing. By employing image fusion algorithms a composite image of the scene over several wavebands can be rendered and convey more information than individual images at each wavelength [1–3].

The complexity and diversity of materials required for imaging different spectral bands mean that modern multi-spectral imaging systems use a range of different cameras. For example, Kowalski et. al used a visible light camera (photodiodes), two IR cameras that operate in the 3-5 μm band and 8-14 μm band (bolometric sensors) and a THz camera (heterodyne detection using a GaAs Schottky mixer) [4]. Such an approach produces high quality images however the set-up is expensive, cumbersome and the acquisition time is long at around 30 minutes. Moreover the majority of image fusion algorithms require that

#254706 Received 30 Nov 2015; revised 26 Jan 2016; accepted 5 Feb 2016; published 10 Feb 2016

the set of images must be spatially aligned i.e. they must represent the exact same scene, presenting a major challenge in accurately exchanging separate detectors in an imaging system. Efforts have been made to reduce the number of components by developing a monolithic solution for the detection of the visible, IR and THz radiation via the co-integration of sensors onto a single CMOS chip. As an example, Perenzoni et. al have developed a 160 x160 pixel CMOS chip that contain Si photodiodes for visible detection and micro-bolometer sensors for IR and THz detection [5]. However the different wavelength sensors are not coaxial and therefore the visible/IR and THz must be detected on different regions of the CMOS chip.

Synthetic multi-spectral materials (SMMs): structured materials capable of operating over different wavebands simultaneously, offer a way to coaxially filter and absorb visible, IR and THz radiation and therefore offer an attractive alternative to conventional detection methods [6–10]. SMMs exploit hybridised metamaterial and plasmonic structures to combine multi-spectral functionalities into a single material. By scaling the plasmonic and MM geometries and selecting the appropriate constituent materials one can realise a universally multifunctional optical material in any waveband from the visible to mm wave. In previous work we have developed SMMs that can: (1) filter visible, near infrared (NIR) and THz [10]; (2) filter visible, NIR and absorb THz [9]; (3) filter visible, NIR and mid IR (MIR) and absorb THz [8] and (4) absorb both MIR and THz [7]. In this paper we demonstrate through simulations and experimentally a SMM capable of filtering 15 visible wavelengths and one NIR wavelength while also absorbing MIR and THz radiation. Such a device could be integrated with a Si CMOS chip where the visible detection would be done by Si photodiodes and the IR/THz detection done by micro-bolometer sensors positioned above the integrated circuit and render a component capable of forming coaxial visible, IR and THz images. This implementation would obviate the traditional approach of using a separate detector material system, typically mercury cadmium telluride (MCT) or indium antimonide (InSb), for the IR detection and flip chip bonding to the CMOS chip used for the visible and THz detection.

In forming the SMM we exploit two optical phenomena, surface plasmon resonance (SPR) and metamaterial (MM) absorption. Surface plasmons (SP) are electron density oscillations at the interface between a dielectric and a conductor. SPs can resonantly couple with incident light to form surface plasmon polaritons (SPP) in a process known as SPR. Periodic subwavelength hole arrays, at optical wavelengths, etched into a thin metal film can excite SPR leading to enhanced transmission and wavelength filtering of the incident light [11, 12]. Colour filters have been fabricated by etching triangular subwavelength hole arrays of varying periods and hole sizes into various thicknesses of aluminium film, sandwiched between two silicon dioxide layers [13, 14]. Plasmonic filters have been optimised for digital imaging by engineering transmission spectra corresponding to the 1931 International Commission on Illumination (CIE) colour matching functions [15] and have also been integrated with CMOS image sensors [16, 17]. Filters fabricated into a metal layer as part of the CMOS process offer a solution to substantial cross-talk between different colours that is expected as CMOS imagers scale to smaller sizes [18]. It is also possible to extend the operation of plasmonic filters to MIR wavelengths by further scaling of the hole size and period [9, 10].

At THz frequencies the plasmonic response is diminished due to the high conductivity of the metal, however MMs can be used instead and also exhibit resonant behaviour [19–22]. MMs are arrays of subwavelength elements, the structure of which rather than their composition, dictates their electromagnetic properties. A MM absorber consists of an electric ring resonator (ERR) array and a metallic ground plane, separated by a sub-wavelength thickness dielectric spacer such as polyimide, silicon dioxide or silicon nitride. At resonance, the ERR couples to the incident electric field and magnetic coupling is provided by the addition of a metallic ground plane, as can be observed by anti-parallel currents on the metal surfaces [23–25]. Resonant and therefore strong absorption only occurs when the impedance of the structure is matched to free space. This implies that $Z = \sqrt{\mu / \varepsilon} = 1$ when normalised to free space. To attain zero reflection the real parts of the effective permittivity and permeability must be zero, while to obtain zero

#254706 Received 30 Nov 2015; revised 26 Jan 2016; accepted 5 Feb 2016; published 10 Feb 2016

transmission whenever the real part of the permittivity is positive the real part of the permeability must be negative and vice versa. Impedance matching only occurs for a narrow bandwidth, dependent on the MM configuration.

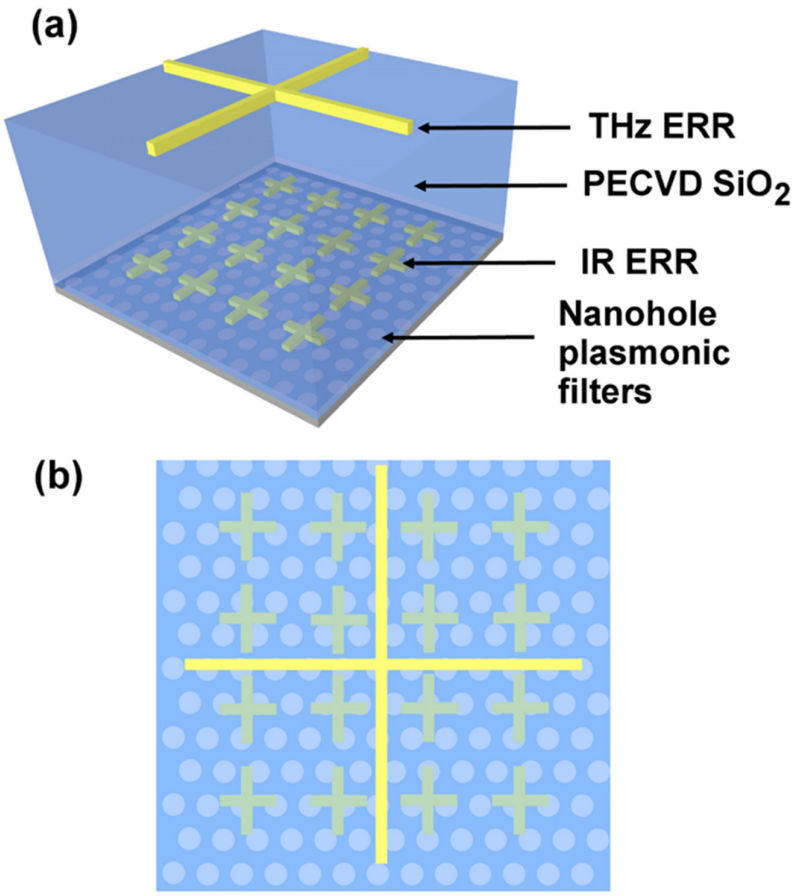

Fig. 1. Illustration of the synthetic multi-spectral material capable of filtering 15 visible wavelengths and 1 NIR wavelength while also absorbing MIR and THz. (a) 3D view and (b) top down view. Note that for clarity and ease of understanding the geometries of the plasmonic filters, MIR ERRs, and THz ERR are not to scale.

By scaling the array period, ERR geometry and insulating layer thickness between the ERR and the ground plane MM absorbers can operate from the IR [26] to the microwave regimes [27]. MM based absorption is inherently narrowband however it is possible to produce a dual band response by adding a second ERR [28] or illicit a broadband response by stacking ERRs on top of one another [29]. The periodic nature of MM absorbers lends itself to coupling with micro-bolometer sensing elements to form a focal plane array (FPA). MM based FPAs have been developed in both the S band (2-4 GHz) [27] and at THz frequencies (2.5 THz) where the MM absorbers were monolithically integrated into a standard 0.35 μm CMOS process and the vanadium oxide micro-bolometer sensors deposited on top [30, 31].

2. Device design and simulation

The SMM described here consists of 16 plasmonic filters fabricated into the ground plane of an MIR and THz MM absorber. The SMM is capable of filtering fifteen optical wavelengths and a NIR wavelength whilst simultaneously absorbing a single MIR frequency and a single THz frequency through exploitation of two unique electromagnetic phenomena. Hybridisation of the MIR MM absorber and THz MM absorber with

#254706 Received 30 Nov 2015; revised 26 Jan 2016; accepted 5 Feb 2016; published 10 Feb 2016

plasmonic filters yields a significant advancement towards the creation of a coaxial multi-spectral imager operating in visible, IR and THz wavelength regimes.

In order to meet the challenge of realising a universal multifunctional material we must be able to accommodate different length scales integrated into a functional lattice block. To do so we hybridise the fractal nature of MM resonators with the alternative SPR function into a 3D crystal. A 3D schematic diagram of the SMM is shown in Fig. 1(a) and a top down view is shown in Fig. 1(b). The lattice unit cell consists of the THz MM absorber. Embedded within are the constituent sub-cells; the MIR ERRs and the nanoholes. The square unit cell period is 40 μm in length and contains 225 MIR ERRs and up to 30000 nanoholes (depending on the hole period). Our SMM is inspired by the structure presented in [9] where visible plasmonic filters are patterned in a 150 nm thick Al film, a 3 μm thick layer of plasma enhanced chemical vapour deposition (PECVD) SiO_2 deposited on top and finally a metallic THz ERR defined. For our new SMM we insert an array of MIR ERRs between the plasmonic filters and the THz ERR. While at first this seems like a trivial modification to incorporate into the stack there are in fact a number of challenges to overcome. For any MM absorber structure the insulating layer thickness between the ground plane and the ERR layer determines the absorption magnitude and the optimum thickness to attain maximum absorption scales with frequency. As an example, when PECVD SiO_2 is used as the insulating layer, at 2 THz the required thickness to obtain 100% absorption is 2 μm however at IR frequencies, e.g. 4 μm, the insulator thickness is only 50 nm [7]. The plasmonic filters require a SiO_2 cap layer thicker than the metal film thickness in order to match the SiO_2-Al modes on both sides of the metal film and therefore maximise the transmission through the filter [13]. For a 150 nm thick Al layer the optimum SiO_2 cap layer thickness is 200 nm however to form a MIR MM absorber at 4 μm the SiO_2 thickness between the ERR and the ground plane is 50 nm. To overcome this challenge we have reduced the Al metal thickness to 50 nm and chosen a 100 nm thick SiO_2 cap layer. Reducing the Al thickness from 150 nm to 50 nm has the effect of increasing the transmission magnitude but also increasing the bandwidth and reducing the spectral contrast [13]. A second challenge we have overcome is minimising the area of the MIR ERRs and the THz ERRs in order to maximise the visible transmission. The metal fill factor of the THz ERR in [9] is 33.6% whereas the THz ERR in our new SMM has a metal fill factor of only 4.3%. The MIR ERR introduced into the stack has a metal fill factor of 20% rendering a total metal fill factor of the new SMM of 24.3%.

The resonant wavelength, λ_{SPP}, for a plasmonic filter triangular hole array is given by Eq. (1):

$$\lambda_{SPP} = \frac{p}{\sqrt{\frac{4}{3}(i^2 + ij + j^2)}} \sqrt{\frac{\varepsilon_m \varepsilon_d}{\varepsilon_m + \varepsilon_d}} \tag{1}$$

where P is the period of the hole array, ε_m is the dielectric constant of the metal, ε_d is the dielectric constant of the dielectric, and i and j are the scattering orders of the array [12, 13]. The sixteen colour plasmonic filter set was designed by scaling the hole size and the array period to shift the resonant wavelength, whilst maintaining similar bandwidths and transmission magnitudes. The MIR and THz MM absorbers geometries were inspired by established designs [7, 25, 26]. The fundamental resonant frequency of a MM absorber based on a cross shaped ERR is [32]:

$$f_m = \frac{1}{\sqrt{LC/2}} \tag{2}$$

where f_m is the resonant frequency position, L in the inductance and C is the capacitance. The capacitance is determined by the area of the ERR and the insulating layer thickness while the inductance is determined by the length and width of the ERR. In effect, the ERR arm length determines the resonant frequency peak position while the thickness of the insulating layer between the two conducting layers determines the absorption

#254706 Received 30 Nov 2015; revised 26 Jan 2016; accepted 5 Feb 2016; published 10 Feb 2016

magnitude [32]. The constituent materials and layer thicknesses of our SMM absorber were altered and optimised for integration with optical plasmonics. The absorption spectrum of the SMM, A(ω), was calculated using Eq. (3):

$$A(\omega) = 1 - R(\omega) - T(\omega) \tag{3}$$

where R(ω) is the reflection spectrum and T(ω) is the transmission spectrum.

The SMM layer structure and composition were optimised by performing simulations using Lumerical FDTD Solutions [33]. The plasmonic filter simulations are set up as follows: a 50 nm Al layer was placed between a semi-infinite SiO_2 layer and a 100 nm silicon dioxide cap layer. The aluminium was patterned with two glass holes and the silicon dioxide cap layer was patterned with two etch holes to account for the cap layer topography after deposition of the silicon dioxide. A mesh grid with a maximum cell size of 5 nm was defined in the vicinity of the holes. Taking advantage of the inherent symmetry of the SMM and to reduce computation demands, symmetric and anti-symmetric boundary conditions were used to form the triangular hole array structure, and perfectly matched layers (PML) were used in the z boundaries. The Al surface was illuminated by a 400 nm to 1 μm plane-wave source and the transmission spectra were recorded by a monitor placed on the opposite side of the Al.

Simulating the MIR MM absorber involved importing the visible plasmonic filter geometry, identical to that described above, and adding a 100 nm thick ERR structure above the silicon dioxide cap layer. The structure was illuminated from above by a plane-wave source. Symmetric and anti-symmetric boundary conditions were once again used in x and y; PML boundary conditions were used in the z-direction. The maximum mesh step size in the region of the ERR was 50 nm in x and y, and 20 nm in z while the maximum mesh step around the plasmonic filter nanoholes was 5 nm in x, y and z. Reflection and transmission monitors were placed above and below the MM unit cell, respectively.

A similar simulation method was used for the THz MM absorber in which the structure was illuminated from above by a plane-wave source. For all MM absorber simulations the electric field was orientated in the x plane. Due to processor memory limitations the plasmonic filter layer was replaced by a continuous metal film however the MIR ERR was still retained. Symmetric and anti-symmetric boundary conditions were once again used in x and y and PML boundary conditions were used in the z-direction. The maximum mesh step size in the MIR ERR region was 50 nm in x and y, and 20 nm in z while the maximum mesh step in the in THz ERR regions was 100 nm in x and y, and 20 nm in z. Reflection and transmission monitors were placed above and below the MM unit cell, respectively.

The disparate wavelength scales from the THz to the visible and the extremely fine mesh required to resolve the nanoholes comprising the plasmonic filters meant that it was impractical to simulate the complete SMM at THz frequencies. Instead, three separate structures were independently simulated and optimised: (1) plasmonic filters only at visible and NIRwavelengths (400-1000 nm), (2) MIR absorber and visible plasmonic filters combined at IR wavelengths (2-6 μm) and (3) THz and MIR MM absorber in the THz range (1-4 THz). Previous work has shown that it is possible to consider the ground plane, constructed of the nanohole plasmonic filters, of the SMM as an unperforated metal film at THz frequencies since less than 10^{-5} of the incident THz wave is transmitted through the nanohole ground plane [9]. At IR frequencies however the wavelength scale approaches the size of the nanoholes and it is necessary to determine if there is significant IR transmission through the structure. Simulations were performed for an MIR MM absorber with a ground plane perforated with the largest nanohole diameter (d = 267.5 nm, period = 550 nm) and revealed a maximum transmission magnitude of 1.4%.

3. Fabrication and device characterisation

The designed SMM absorber consisted of a 50 nm thick aluminium layer, into which was patterned the nanohole array, a 100 nm SiO_2 cap layer and a 10/90 nm Ti/Au MIR ERR separated by a 4 μm thick SiO_2 spacer from the 10/90 nm Ti/Au THz ERR. This in effect

#254706 Received 30 Nov 2015; revised 26 Jan 2016; accepted 5 Feb 2016; published 10 Feb 2016

meant that there was 100 nm of SiO_2 between the Al layer and the MIR ERR, forming the MIR MM absorber, and 4.1 μm of SiO_2 between the Al layer and the THz ERR, forming the THz MM absorber. SiO_2 was chosen as the dielectric spacer material as it exhibits low loss at optical and near IR wavelengths. The MIR ERR cross geometry is as follows: p_1 = 2 μm, l_1 = 1.2 μm, w_1 = 0.4 μm and the THz ERR geometry is p_2 = 40 μm, l_2 = 35 μm, w_2 = 1 μm. Standard electron beam lithography techniques were used to define the nanoholes for the plasmonic filters and the IR and THz ERRs. The MM absorber ground plane consisted of sixteen plasmonic filters. Each filter was 1 mm x 1 mm in size and was separated from neighbouring filters by 0.33 mm; the sixteen filters extended to a square area of 5 mm x 5 mm. The hole diameters of each of the filter arrays were measured prior to deposition of the 100 nm thick SiO_2 cap layer.

A SEM image of a red plasmonic filter (P = 430 nm) is shown in Fig. 2(a) and 2(b). The MIR and THz ERR arrays covered an area of 12 mm x 12 mm over the plasmonic filters. Transmission microscope images of the completed SMM are shown in Fig. 2(c) and 2(d). Figure 2(c) shows the THz ERR array above the blue plasmonic filter ground plane section and Fig. 2(d) shows the THz ERR array above the red plasmonic filter ground plane sections, respectively. A SEM of the MIR ERRs is shown in Fig. 2(e). Figure 2(f) shows a tessellated picture of the SMM surface. Note that the ERR structures are not resolved.

The spectral characteristics of the SMM were investigated in detail using sources and detectors appropriate to the wavelengths of interest. The optical and NIR transmission spectra from the plasmonic filter sections of the SMM were measured using a TFProbe MSP300 microspectrophotomer with a white light halogen lamp source and a detector with a spot size of 100 μm. The transmission spectra were normalised to the white light source. Characterisation of the MIR and THz MM absorber component of the SMM was performed using a Bruker IFS 66v/S Fourier transform infrared spectrometer (FTIR) in reflection mode at 30° incidence. For the IR region the reflection and transmission measurements were performed using a SiC globar source, KBr beamsplitter and a deuterated L-alanine-doped triglycine sulfate (DLATGS) pyroelectric detector. The THz measurements required the use of an Hg source, a Mylar beamsplitter, and a DLATGS detector with a polyethylene window. The reflection spectrum was normalised to a gold mirror through a 10 mm aperture.

#254706 Received 30 Nov 2015; revised 26 Jan 2016; accepted 5 Feb 2016; published 10 Feb 2016

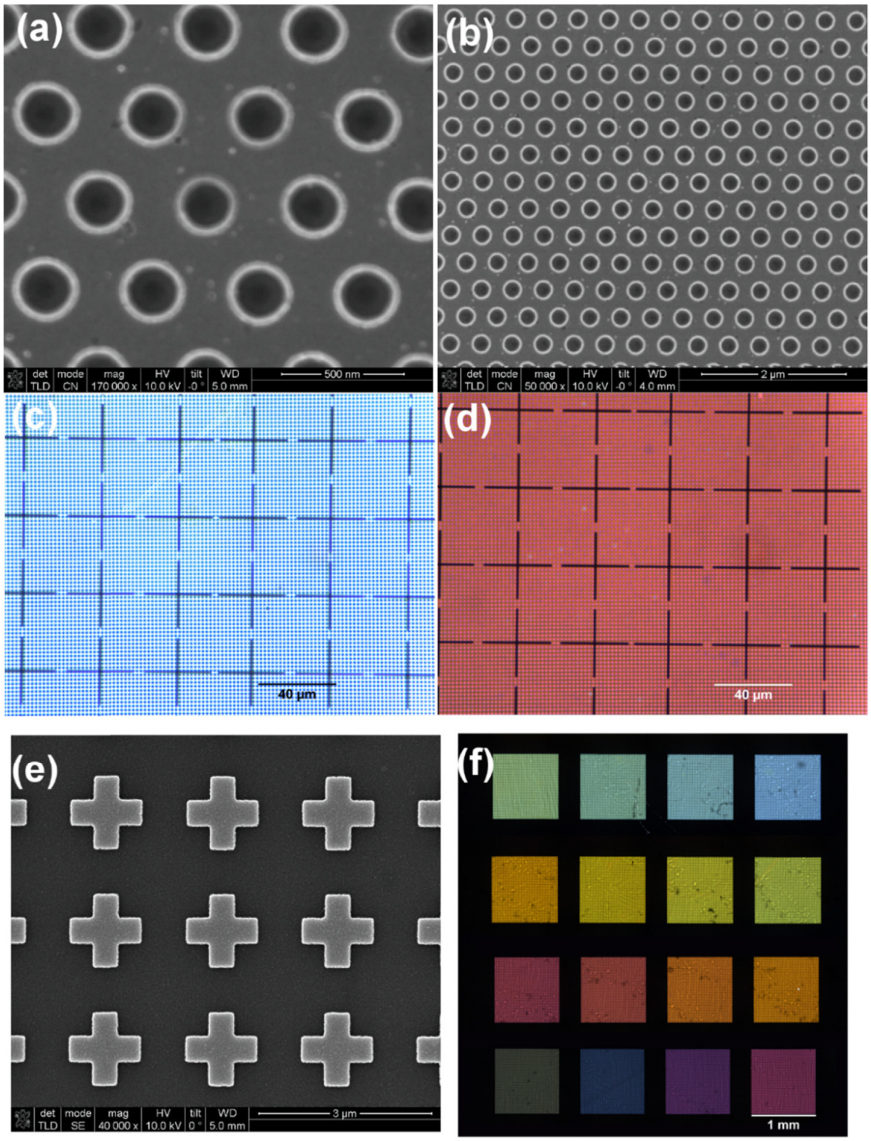

Fig. 2. Scanning electron micrographs of a plasmonic filter hole array and MIR ERRs and transmission microscope images of the synthetic multi-spectral material (SMM). (a)-(b) Scanning electron micrographs of a red plasmonic filter (P = 430 nm) at different magnifications. Transmission microscope images showing electric ring resonators (ERRs) above (c) a blue plasmonic filter (P = 230 nm) and (d) a red plasmonic filter (P = 410 nm). (e) SEM of the MIR ERRs. (f) Tessellated transmission microscope image of the region of the SMM covered with plasmonic filters. This type of colour swatch is commonly employed to display the colour filtering properties across the visible spectrum. The MIR and THz ERRs are not visible in the image however they result in a decrease in intensity of the plasmonic filter transmission spectra.

#254706 Received 30 Nov 2015; revised 26 Jan 2016; accepted 5 Feb 2016; published 10 Feb 2016

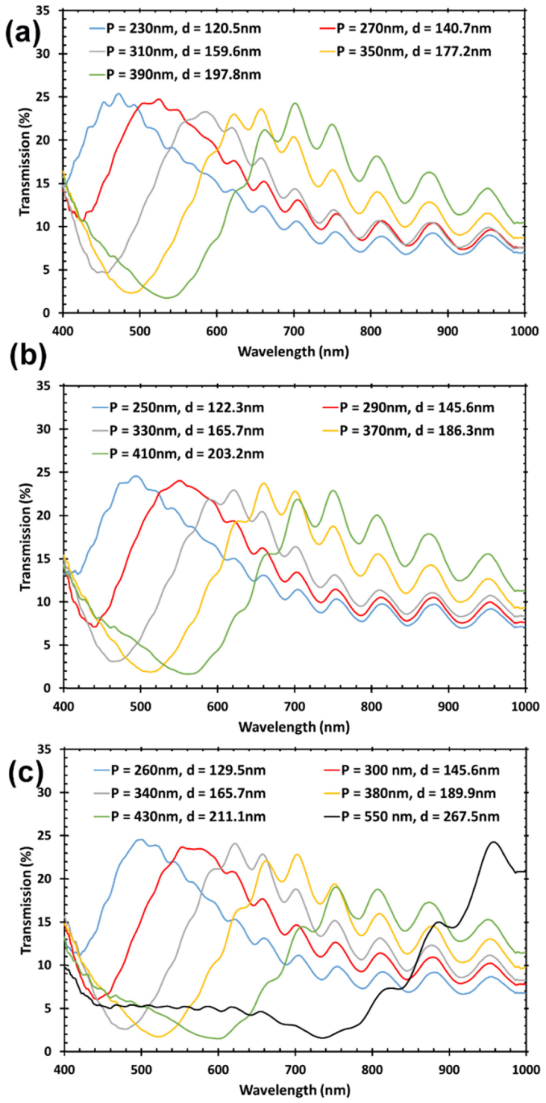

Fig. 3. Measured spectral characteristics of the synthetic multispectral material (SMM). The transmission spectra associated with the plasmonic filters are shown in (a)-(c). The hole period, *P*, and hole diameters, *d*, as measured using a scanning electron microscope (SEM) are shown in the legend.

4. Results

The transmission spectra from the plasmonic filter regions of the SMM are shown in Fig. 3(a)-3(c). The legend denotes the hole period and the measured hole diameters of each filter. Fabry-Perot oscillations appear in the transmission spectra due to the silicon dioxide dielectric spacer. The peaks are consistent over all colour filters and correspond to a 4.1 μm resonator cavity with refractive index: n = 1.48 [34]. The transmission and reflection spectra of the SMM at MIR and THz frequencies were measured and, using Eq. (2), it was possible to calculate the absorption spectrum, shown in Fig. 4(a)-4(c). Bespoke MIR and THz MM absorbers constructed only of the metal ground plane/SiO_2/ERR stack were also simulated, fabricated and characterised in order to fully understand the rich absorption spectrum of the SMM. In the 2-6 μm region, shown in Fig. 4(b), the simulated standalone MIR ERR absorber has a single resonant absorption peak of magnitude 81% at 4.02 μm. The absorption spectrum of the fabricated standalone MIR MM absorber shows

#254706 Received 30 Nov 2015; revised 26 Jan 2016; accepted 5 Feb 2016; published 10 Feb 2016

good agreement with the simulation data, having an absorption magnitude of 98% at 4.14 μm. The absorption spectrum of the SMM was measured after fabrication of the MIR ERR layer and also on completion of the device by adding the 4 μm SiO_2 and THz ERR. At the MIR ERR stage the SMM has an absorption magnitude of 91% at 4.30 μm while on completion of the device fabrication the peak absorption redshifted to 4.56 μm and the absorption magnitude remained the same at 91%. A second prominent absorption peak of 81% magnitude at 2.75 μm is present in the SMM absorption spectra. This peak is also present in the spectral characteristics of the fabricated standalone THz MM absorber indicating that its origin is directly related to the addition of the 4 μm SiO_2 and the THz ERR layers. The simulated data has an absorption peak of 95% magnitude at 2.80 THz however the experimental spectrum has an absorption peak of magnitude 53% at 2.37 THz. The experimental data of the SMM has similar spectral characteristics to the standalone THz MM absorber having an absorption peak at 2.38 THz of 51%. The discrepancy between the simulated and experimental spectra of the standalone THz MM absorber is likely due to an error in the simulated complex refractive index of the SiO_2 layer. The simulation used book values from Palik [35] however the PECVD SiO_2 deposited in our facility is likely to be much different. PECVD SiO_2 films are known to have large concentrations of impurities such as hydrogen and nitrogen [36]. Incorporation of such impurities into PECVD SiO_2 films are likely to increase both the refractive index and the loss tangent at THz frequencies. Accurately determining the refractive index of materials at THz frequencies using techniques such as THz time domain spectroscopy requires films at least λ/5 thick [37]. In our case the film thickness of the PECVD SiO_2 is ~λ/25 making it impossible to evaluate experimentally. Instead we have empirically modified the Palik SiO_2 material parameters such that the simulated absorption spectrum better matches the experimental data (see Fig. 4(b)). In doing so the SiO_2 refractive index has increased from 1.96 to 2.4 while the loss has increased from ~0.01 to 0.2.

Figure 4 (c) shows the spectral characteristics of the SMM from 1 to 1000 THz corresponding to 300 μm to 300 nm. Also shown is the simulated absorption spectrum for a standalone THz MM absorber with a SiO_2 spacer thickness of 4.1 μm. As already mentioned, due to excessive computation demands it was not possible to simulate the full SMM structure. In total we identify 13 absorption peaks, labelled A-M. By examining the electric and magnetic field distributions at each of the peaks we are able determine the nature of the absorption for almost all of the absorption peaks. Figure 5 shows the electric and magnetic field distribution for the peaks labelled A, B, C, M and K. The electric field profile in Fig. 5(a) shows excitation of the fundamental dipole mode of the THz MM absorber, corresponding to opposite charges accumulating at the edges of the x-axis orientated cross arm. The magnetic field distribution shown in Fig. 5(b) clearly indicates the excitation of the magnetic dipole in the SMM which is caused by oppositely oriented currents on the THz ERR and the ground plane. The electric field and magnetic field profiles shown in Fig. 5(c)-5(f) reveal that at peaks B and C higher order modes of the THz MM are excited resulting in resonant absorption. The simulation data shows strong absorption magnitudes for modes B and C however experimentally they only appear as shoulders of a more broader absorption peak. This anomaly is most likely due to the aforementioned discrepancy between the simulated and experimental SiO_2 refractive index. Figure 5(g) and 5(h) show the electric field and magnetic field distribution for peak F. There is no resonant response implying that the absorption is due to classical dielectric absorption in the PECVD SiO_2 layer. Indeed all the absorption peaks from D-I are due to classical dielectric absorption. Turning to the MIR region, peak K is due to excitation of the fundamental IR MM absorber mode (see Fig. 5(i) and 5(j)) while peaks J, L and M are tentatively ascribed to dielectric absorption caused by impurities in the PECVD SiO_2. For completeness, also highlighted is the transmission peak for the blue plasmonic filter (period = 230 nm, diameter = 120.5 nm).

#254706 Received 30 Nov 2015; revised 26 Jan 2016; accepted 5 Feb 2016; published 10 Feb 2016

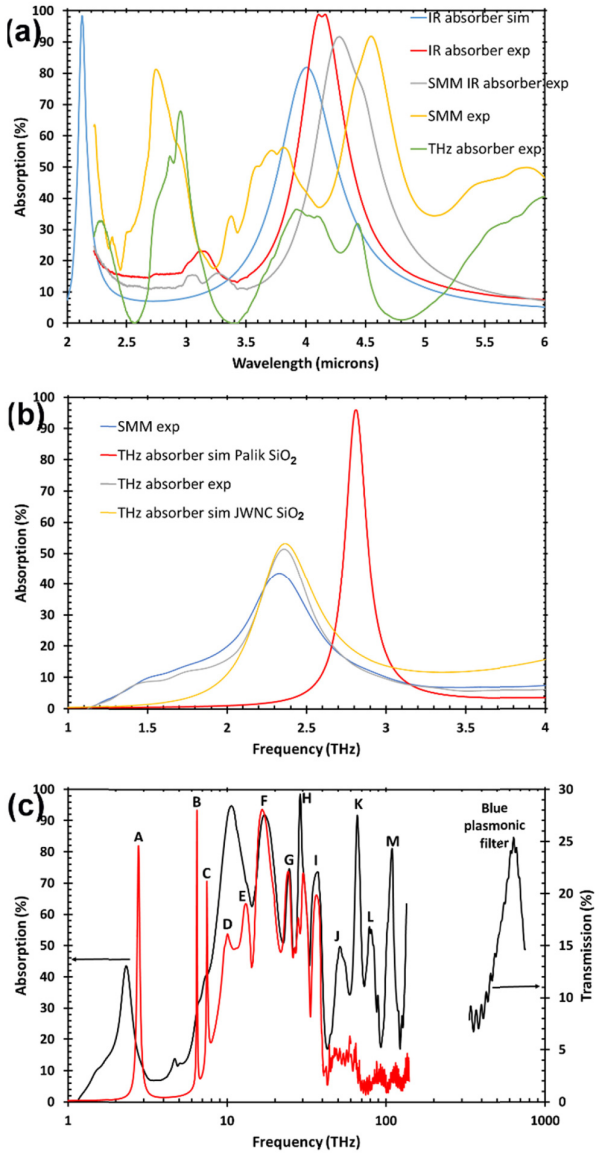

Fig. 4. Experimental and simulated spectral characteristics of the synthetic multi-spectral material (SMM). (a) Experimentally and simulated measured absorption spectra in the 2-6 μm region for the SMM, a standalone MIR absorber and a standalone THz absorber. (b) Experimentally and simulated THz absorption spectra of the SMM compared with a standalone THz MM absorber of the same design, but without a perforated ground plane and the MIR ERRs. (c) Black line - Complete experimental spectrum from 1 THz (300 μm) to 1000 THz (300 nm) of the SMM. Red line – Simulated absorption spectrum from 1 THz (300 μm) to 140 THz (2.14 μm).

#254706 Received 30 Nov 2015; revised 26 Jan 2016; accepted 5 Feb 2016; published 10 Feb 2016

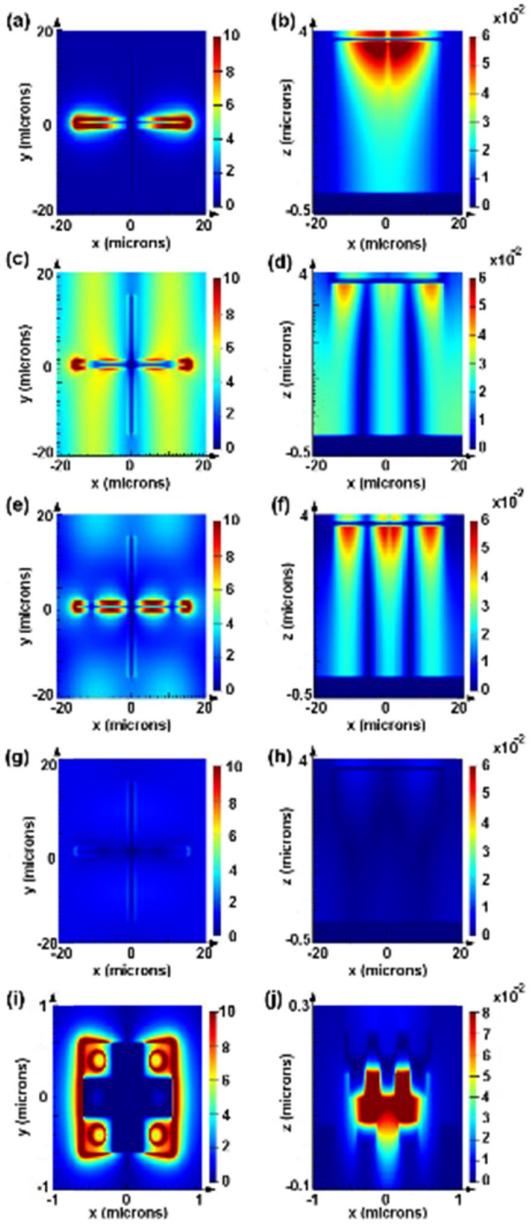

Fig. 5. Electric and magnetic field distributions of the SMM at absorption peaks A, B, C, M and K. (a), (c), (e), (g) and (i) represent the electric field in the THz ERR, (b), (d), (f), (h) and (j) represent the magnitude of the magnetic field in the multi-layer structure.

5. Conclusion

In this article we have demonstrated the design, fabrication and characterisation of a new type of SMM that hybridises optical plasmonic filters with a MIR MM absorber and a THz MM absorber to combine multiple functionalities as well as multi-spectral capabilities into a single material. Our device exhibits multiple functionalities by incorporating the MIR MM absorber and colour filter structure within a standard THz MM absorber. The SMM combines fifteen colour plasmonic filters, a single NIR plasmonic filter, a frequency selective MIR MM absorber and a frequency selective THz MM absorber. Our device demonstrates that the presence of plasmonic filter hole arrays

#254706 Received 30 Nov 2015; revised 26 Jan 2016; accepted 5 Feb 2016; published 10 Feb 2016

in a THz MM absorber ground plane has negligible impact on the MIR and THz absorption spectrum associated with the MM absorbers.

A natural application for our SMM device is in multi-spectral imaging. The periodic nature of MM and plasmonic structures naturally lends itself to forming arrays and more specifically focal plane arrays. The plasmonic filters can be used in conjunction with photodiodes and the MIR and THz MMs can be combined with a detector material, for example a micro-bolometer, therefore demonstrating a clear path for integrating a multi-spectral material with a CMOS imaging chip to create a multi-spectral camera. The SMM we have developed here could form a colour image and images at 4.5 μm and 126 μm (2.37 THz) however by selecting the appropriate materials and device geometries images could be formed at any waveband between the visible and THz. Image fusion, the process of combining relevant information from two or more images into a single image, would render a resulting image that is more informative and data rich than either of the individual input images.

Acknowledgments

We thank the staff of the James Watt Nanofabrication Centre at the University of Glasgow for assistance in fabricating the devices reported in this paper. J.G. also acknowledges fruitful discussions with E.W. Burnett. This research was funded from EPSRC grants EP/I017461/1 and EP/J018678/1.

#254706 Received 30 Nov 2015; revised 26 Jan 2016; accepted 5 Feb 2016; published 10 Feb 2016